

Article

Optimization of Pin Type Single Screw Mixer for Fabrication of Functionally Graded Materials

Shijie Wang ¹, Jing Zhou ² and Guolin Duan ^{1,*}¹ School of Mechanical Engineering, Hebei University of Technology, Tianjin 300401, China; leonhebut@163.com² School of Mechanical Engineering, Tianjin University of Science and Technology, Tianjin 300457, China

* Correspondence: glduan@hebut.edu.cn; Tel.: +86-135-0213-0628

Abstract: The direct ink writing (DIW) process, used for creating components with functionally graded materials, holds significant promise for advancement in various advanced fields. However, challenges persist in achieving complex gradient variations in small-sized parts. In this study, we have developed a customized pin shape for an active screw mixer using a combination of quadratic B-Spline, the response surface method, and global optimization. This tailored pin design was implemented in a two-material extrusion-based printing system. The primary objective is to facilitate the transformation of material components with shorter transition distances, overcoming size constraints and enhancing both printing flexibility and resolution. Moreover, we characterized the transition delay time for material component changes and the mixing uniformity of the extruded material by constructing a finite element simulation model based on computational fluid dynamics. Additionally, we employed a particle tracking method to obtain the Lyapunov exponent and Poincaré map of the mixing process. We employed these metrics to represent and compare the degree of chaotic mixing and dispersive mixing ability with two other structurally similar mixers. It was found that the optimized pin-type mixer can reduce the transition delay distance by approximately 30% compared to similar structures. Finally, comparative experiments were carried out to verify the printing performance of the optimized pin-type active mixer and the accuracy of the finite element model.

Keywords: direct ink writing; functionally graded materials; transition delay distance; chaotic mixing; pin type active mixer



Citation: Wang, S.; Zhou, J.; Duan, G. Optimization of Pin Type Single Screw Mixer for Fabrication of Functionally Graded Materials. *Appl. Sci.* **2024**, *14*, 1308. <https://doi.org/10.3390/app14031308>

Academic Editor: Arkadiusz Gola

Received: 15 January 2024

Revised: 1 February 2024

Accepted: 3 February 2024

Published: 5 February 2024



Copyright: © 2024 by the authors. Licensee MDPI, Basel, Switzerland. This article is an open access article distributed under the terms and conditions of the Creative Commons Attribution (CC BY) license (<https://creativecommons.org/licenses/by/4.0/>).

1. Introduction

The landscape of industrial applications has evolved to become more diverse and demanding, presenting challenges for the effectiveness of single-material parts in complex scenarios [1,2]. Therefore, a novel type of composite material, termed functionally graded materials (FGMs), which comprise two or more materials, has emerged and is drawing significant academic interest. FGMs are characterized by their material compositions varying spatially through customized gradients, leading to exceptionally satisfactory histocompatibility. This strategic composition mitigates the issue of abrupt interfaces between materials, thus enabling the full exploitation of the inherent potential of each material [3–5]. Specifically, ceramic-based FGMs, when integrated with flexibility-oriented additive manufacturing processes, are becoming increasingly crucial in a variety of critical fields, including military [6–8], bioengineering [9–12], energy [13,14], and aerospace [15–18].

During the last two decades, the field of additive manufacturing (AM) technology has made significant advancements. Layer-based AM processes for the preparation of FGM parts primarily emphasize flexibility and customization. This approach enables the incorporation of both geometric gradients and varying material compositions. For most ceramic-based FGMs, the raw material exists primarily in a liquid phase. Direct ink writing (DIW), as a distinctive form of Directed Energy Deposition (DED), proves to be

a potent method for preparing liquid-phase FGMs [19]. In addition, DIW demonstrates high applicability across a wide range of liquid-phase materials and offers economic efficiency. Therefore, DIW has been widely adopted in the field of ceramic-based FGM manufacturing [20–22].

The workflow of DIW involves raw material preparation, real-time mixing, and extrusion of mixed materials. Among these steps, rapidly achieving uniform mixing of multi-pastes is crucial when producing composite materials with gradients. Ceramic pastes possess highly viscous properties, which makes mixing challenging. The mixing of highly viscous fluids primarily occurs in a laminar flow in the mixing mechanism, which significantly impedes mixing efficiency. Simultaneously, in the context of the continuous extrusion DIW process, the time required for various proportions of multi-materials to achieve homogeneous mixing in the mixing chamber results in a delay in the transition of printed material composites. This directly impacts the printing resolution [23]. Therefore, it is imperative to optimize the efficiency of the mixing process, minimize the transition delay distance, and enhance print resolution to achieve intricate gradient variations in compact components. It is worth noting that some researchers have successfully prepared ceramic-based FGM parts using static mixers [24,25] or dynamic mixers [26]. Additionally, Computational Fluid Dynamics (CFD) methods have been employed to analyze the fluid dynamics in the mixing chamber. Despite the increased control demands associated with active mixers, they demonstrate superior mixing capabilities in comparison to static mixers. This results in enhanced print resolution and a more streamlined printing system.

The screw mixer represents an active mixing mechanism known for its exceptional back-mixing and transportation capabilities. It has found widespread utilization in multi-material mixing and extrusion processes due to its simple design and low-maintenance advantages [27,28]. A typical screw serves to prolong the material's residence time in the mixing chamber through back-mixing, thereby enhancing the homogeneity of mixed multi-materials. Nevertheless, when preparing FGMs using the DIW process and needing to change material components to improve print resolution while ensuring homogeneous mixing, it becomes crucial to reduce the required mixing time. Therefore, standard screw mixers are unsuitable for processing FGM parts.

Chaotic mixing proves to be the most effective method for enhancing the mixing efficiency of high-viscosity fluids [29]. The emergence of chaotic mixing effects enhances the radial mixing capacity of the screw while reducing axial mixing along the extrusion direction, facilitating the swift completion of material composite transformation [30–32]. Uncomplicated screw mixers excel in axial mixing abilities but are insufficient in generating chaotic mixing effects, which are essential in FGM preparation. In response to this constraint, some researchers have employed more complex differential twin-screw or tri-screw structures to induce chaotic mixing and thereby enhance mixing efficiency [33–39]. Nevertheless, the resulting complexity in the mixing mechanism poses challenges in the accurate control of printed material components and leads to increased assembly requirements and an unwieldy printing system [40]. In an effort to induce chaotic mixing in a simple single-screw structure, Kim and Wiggins et al. developed a novel single-screw mixer with rectangular pins. The existence of chaotic mixing effects induced by this pin-type single screw was confirmed through experiments and numerical analysis [41–44]. Nonetheless, the optimal pin profiling remains an area of exploration, and there is untapped potential in both the regular rectangular pins and structural parameters of the single-screw to further enhance the chaotic mixing effect, thus improving print resolution.

The Response Surface Method (RSM) represents a valuable statistical method ideally suited to address complex multivariate issues. In this context, the Central Composite Design (CCD) approach proves highly effective in analyzing complex factor interactions, thereby facilitating the derivation of a comprehensive and efficient response function. For instance, Park utilized CFD in the framework of the RSM method to optimize screw parameters, enhancing both drying efficiency and self-cleaning capabilities [45]. Likewise, in the domain of food engineering, optimization of relevant screw parameters resulted in

improved extrusion efficiency [46]. Additionally, the CCD method was utilized to construct a significant response function for fundamental screw parameters, with the primary objective of evaluating the uniformity of grass seed mixing [47]. These instances highlight the remarkable applicability of the RSM method in addressing the optimization challenges presented by multiple factors in the structural parameters of tailored screw mixers.

In response to these challenges, the primary objective of the present work is to design a specialized pin-type single-screw mixer tailored for use in DIW processes. This mixer aims to reduce the transition delay distance in material composites' transformation and enhance print resolution. Contemporary computer-based optimization design methods offer an alternative to the traditional trial-and-error approach, which heavily relies on designer experience and is time-intensive. Hence, this research employs a combination of data-driven and simulation approaches to develop an efficient pin pattern. Initially, an active mixing chamber's digital model, based on CFD in ANSYS FLUENT, is created. This model simulates the mixing time of an active online flow of FGMs. The transition time for gradient changes is assessed by monitoring the volume fraction change of the mixed fluid at the outlet of the mixing chamber, thus obtaining the gradient material's transition regularity at various ratios during the DIW process. Thereafter, the pin's shape is parametrically defined using a quadratic B-spline, and the optimal pin morphology is determined by integrating RSM with a genetic algorithm (GA), with the aim of achieving the shortest transition time. Additionally, the degree of chaotic mixing in the customized pin-type screw can be assessed in the digital model by tracking particle traces and calculating the Lyapunov exponent [48]. The final stage of this study involves experimental validation using a self-developed FGM-printing prototype equipped with dual extruders operating at different feed rates. Two pastes are extruded at distinct feed rates into the dynamic mixing chamber, where they are continuously blended by the customized pin-type screw mixer and subsequently delivered to the extrusion needle. This process is supported by a movable platform to create FGM samples. The effectiveness of the optimized pinned mixer is confirmed through digital image processing methods, demonstrating that the tailored pin-type single-screw mixer can achieve shorter transition distances in the printed samples.

2. Materials and Methods

In this section, the modeling of the mixing chamber was detailed using ANSYS FLUENT Vision 2020R2 (fluid simulation software) as the initial step. Thereafter, the volume fraction of the mixed material at the outlet and the uniformity of mixing under a specific feed rate ratio for two input materials were monitored to assess the screw mixing performance. Following this, the response function corresponding to the transition delay time was derived with the RSM in conjunction with the feasible position of the screw pin control point. Finally, to determine the optimal pin pattern, the response function was optimized through a genetic algorithm. The effectiveness of this optimized pattern was then verified by comparing the results with simulation data, with a particular focus on identifying discrepancies.

2.1. Governing Equations

In kinetic analysis, a fluid can be regarded as a continuous medium, and its motion adheres to the principles of conservation of mass, momentum, and energy. Among these principles, the conservation of energy is commonly employed for calculations in systems involving heat exchange flows. For the mixing and extrusion processes conducted at room temperature in this study, the mixing pastes were considered incompressible, and heat transfer in the mixing chamber was considered negligible. In addition, the two pastes utilized in this study are classified as non-Newtonian fluids due to their high viscosity. Thus, it was assumed that heat transfer could be disregarded under isothermal conditions, while the influence of gravity was taken into account. The flow of incompressible multicomponent viscous slurries was described using the simplified Navier–Stokes equations [49]. Finally,

the continuity equation and momentum conservation equation governing fluid motion are depicted in Equations (1) and (2), respectively.

$$\nabla \cdot (\rho v) = 0 \tag{1}$$

$$\rho \frac{\partial v}{\partial t} + \rho v \cdot \nabla v = -\nabla p + \nabla \cdot \tau + G \tag{2}$$

where ρ represents the fluid density with unit of kg/m^3 , v is fluid velocity. p stands for static pressure on the fluid, and t is time. τ indicates the stress tensor, and G is the gravity.

2.2. Finite Element Model

As illustrated in Figure 1a, a dual-extruder system was employed to combine varying feed volume flow rates, using a motor-driven active mixer, to realize the DIW process for printing FGM parts. The primary component in the mixing chamber, the pin-type screw mixer, plays a pivotal role in this process. It possesses specific dimensions, including a length of 60 mm, a minor screw diameter of 6 mm, a pitch of 8 mm, and a flight width of 1 mm. To ensure effective mixing, a shallow screw groove with a depth of 1 mm was incorporated [50]. The customized pin shape was derived using a quadratic B-spline curve featuring three control points. These control points were defined based on their respective coordinates in the local map shown in Figure 1a. To prevent the co-linearity of the three control points, the coordinates of the first control point were established in relation to the third control point. The ranges of these three control points are detailed in Table 1. It is crucial to emphasize that, to guarantee the uniqueness of the quadratic B-spline generated from these three control points, this research utilized an interpolator in the Unigraphics NX 12.0 software, incorporating neither slope nor curvature constraints. Therefore, the sequence of control point insertion ensured the uniqueness of the generated spline curve. The pin height was set at 1 mm, matching the screw flight height. In addition, we evenly distributed thirty pins around the screw to enhance mixing quality [51].

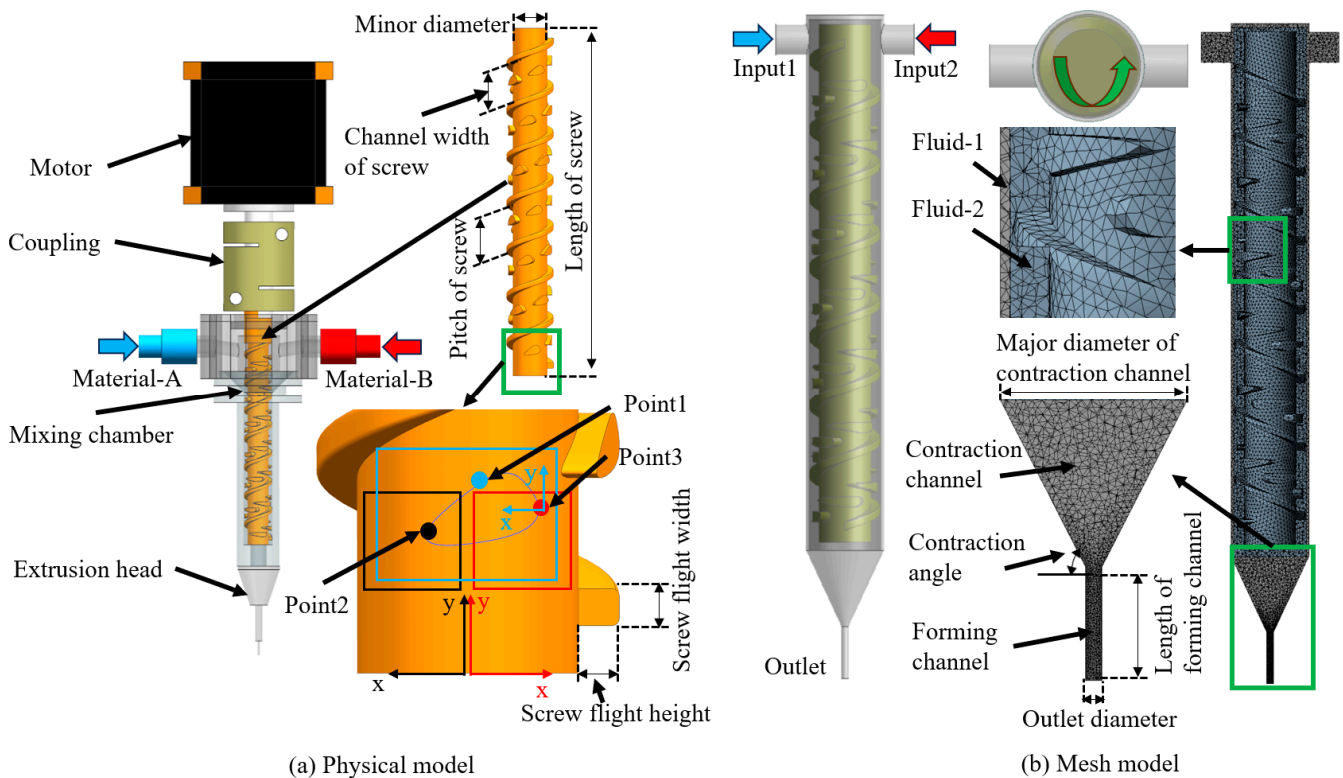


Figure 1. Illustration of: (a) physical model and (b) mesh model of mixing chamber.

Table 1. Range of coordinate values for the three control points.

	x-Axis	y-Axis
Point 1	0.5~2 mm	0.1~1 mm
Point 2	0.5~2.5 mm	3~5 mm
Point 3	0.5~2.5 mm	3~5 mm

As illustrated in Figure 1b, we depicted the numerical simulation model for the mixing component in a mixing chamber equipped with a custom pin-type single screw structure. The screw is configured to rotate clockwise, with a counterclockwise direction of operation. In addition, two parameters are defined in the model to simulate varying material ratios, while a single outlet is designated to emulate the extruded mixing fluid. Details regarding the structural parameters of the finite element model for the mixing chamber can be found in Table 2.

Table 2. Structural parameter of mixing chamber mesh model.

Name	Value [Unit]
Length of screw	60 mm
Minor diameter of screw	6 mm
Pitch of screw	8 mm
Screw flight width	1 mm
Channel width of screw	7 mm
Screw flight height	1 mm
Pin height	1 mm
Input diameter	2.5 mm
Outlet diameter	1 mm
Contraction angle	65°
Major diameter of contraction channel	9 mm
Length of forming channel	6 mm

During the meshing process, the screw mixer structure is treated as a solid medium, and the remaining portion of the mixing chamber structure is designated as a fluid domain. Notably, the flow of the medium is significantly more vigorous in this region compared to other sections of the mixing chamber, owing to the narrow gap between the chosen screw structure and the inner wall. An unstructured tetrahedral mesh tailored to the irregular spatial characteristics is employed for meshing the fluid domain of the mixing chamber to enhance the accuracy of the calculations. Specifically, the boundary layer mesh is optimized, with local densification observed at the inputs, the boundaries of the rotational domain, and the contraction channel. Finally, a mesh size of 0.2 mm is applied to the rotational domain, while the rest of the region employs a mesh size of 0.3 mm. This results in approximately 1.753 million elements and 0.372 million nodes. It should be noted that the number of elements and nodes may slightly vary due to the different pin control points defined.

2.3. Simulation Settings and Paste Properties

To obtain a definitive solution for the flow field, it is necessary to establish the initial boundary conditions in the simulation domain. When preparing FGM parts with extrusion technology, a pressure-based solver was chosen to analyze the low-velocity, incompressible flow field. The boundary conditions were set separately for the velocity inlet and pressure outlet. The combined feed rate for the two inputs was held constant at 0.5 mm/s. Therefore, the total volumetric flow rate could be determined by calculating the cross-sectional area of

the inlet, resulting in a value of $2.4 \text{ mm}^3/\text{s}$. To simulate the rotating flow field in the mixing zone of the pin-type screw, the transient simulation employed the Rotating Reference Frame (RRF) method. This involved designating Fluid-1 and Fluid-2 (as depicted in Figure 1b) as static and dynamically rotational domains, respectively, with both domains being connected through an interface. In addition, the screw wall was assigned a no-slip boundary condition and was configured as a moving wall to simulate the adjustable operating speed of the screw, ranging from 10 to 50 rpm.

In this research, we employed two readily available types of calcium carbonate-based toothpaste, designated as Material A (white color) and Material B (green color), with similar non-Newtonian rheological properties to simulate the mixing extrusion process. The densities of Materials A and B were determined to be 1120 kg/m^3 and 1285 kg/m^3 , respectively, using the specific gravity method. Both pastes exhibit shear-thinning rheological characteristics. Therefore, the study employed the power-law function, as shown in Equation (3), which is a commonly utilized tool in non-Newtonian fluid modeling, to describe their rheological properties. The rheological parameters for both pastes were assessed using a rotational rheometer (MCR 302, Anton Paar, Graz, Austria) at room temperature. The test results are depicted in Figure 2, and the corresponding rheological parameters were derived through the power-law function, as presented in Table 3. Finally, in the confines of a narrow mixing channel, in conjunction with the aforementioned pin-type screw speed, the viscous behavior of the mixing paste was characterized as laminar flow.

$$\tau = K(\dot{\gamma})^n \quad (3)$$

where τ is the shear stress with unit of Pa, K represents the flow index with a unit of $\text{Pa} \cdot \text{s}^n$, and n symbolizes the dimensionless flow behavior index, which is less than 1 for shear thinning paste. $\dot{\gamma}$ is the shear rate with a unit of s^{-1} .

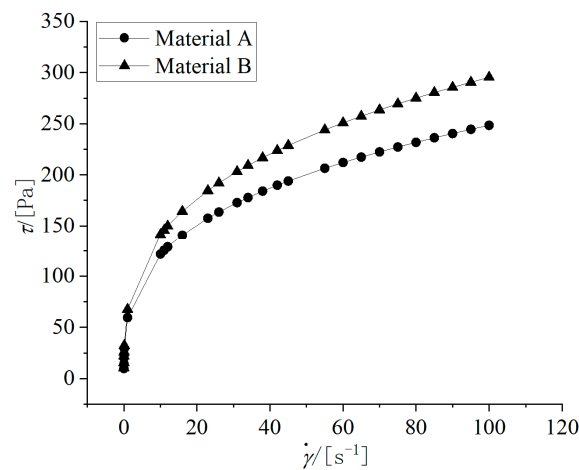


Figure 2. Rheological property curves of two pastes.

Table 3. Rheological parameters of two pastes.

	K	n
Material A	59.59	0.31
Material B	67.68	0.32

2.4. Response Surface Method and Optimization

We employed a second-order RSM design with rotational center composites to achieve significant and highly fitting and accurate statistical results with a limited number of experiments. This design aimed to establish the response function of six coordination variables concerning transition delay time. Thereafter, global optimization was conducted

using a genetic algorithm in conjunction with a robust predictive model to identify the optimal pinning pattern. The optimization process is illustrated in Figure 3. Considering the feasible range of the three control points on the surface of the screw minor diameter, their variable boundaries were determined based on star points. Therefore, following the methodology of the rotatable CCD, a six-factor half-quantity experiment was conducted to calculate the normalized distance α from the design centroid to the boundary points of the design space, as described in Equation (4). Table 4 provides information on the range of coordination variable levels for the three control points.

$$\alpha = (2^{F-1})^{\frac{1}{4}} \quad (4)$$

where F is the number of factors.

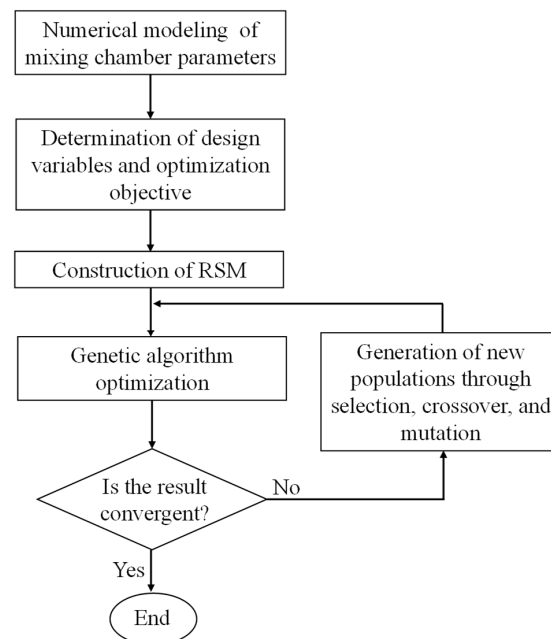


Figure 3. Optimization flowchart based on the RSM and genetic algorithm.

Table 4. Five-level rotatable central composite design.

		Coded Levels				
		−2.378	−1	0	+1	+2.378
Point 1	x-axis	0.5	0.93	1.25	1.57	2
	y-axis	0.1	0.36	0.55	0.74	1
Point 2	x-axis	0.5	1.08	1.5	1.92	2.5
	y-axis	3	3.58	4	4.42	5
Point 3	x-axis	0.5	1.08	1.5	1.92	2.5
	y-axis	3	3.58	4	4.42	5

The response variable for the design experiment was set as the delay time corresponding to scenarios with the most challenging material ratio changes, with the aim of investigating the beneficial impact of varying pin patterns on reducing transition delay time [24]. This scenario represents the highest print resolution achievable. Initially, the material ratio in the mixer chamber was defined as 9:1 for material A to material B, with input feed ratios set at 1:9 while maintaining a total feed rate of 0.5 mm/s. The simulation process maintained a constant screw speed of 25 rpm, consistent with the subsequent experimental phase. The volume fraction of material A at the outlet was continuously

monitored and recorded. The tolerance for the component transformation spanned $\pm 5\%$. In other words, the time interval corresponding to a change in the material A component from 0.86 to 0.14 represented the transition delay time. Figure 4 presents a simulation result for the Nr.35 experimental design condition, illustrating the transition delay time for material mixing transformations and the evolving mixing conditions in the chamber at different time points. In addition, the software Design-Expert 13.0 generated a total of 52 conditional values for the six-factor half-quantity design points, including eight center points. These values were established based on the aforementioned simulation setup to obtain the response values, specifically the transition delay time. The design experiment points and response results are detailed in Table 5.

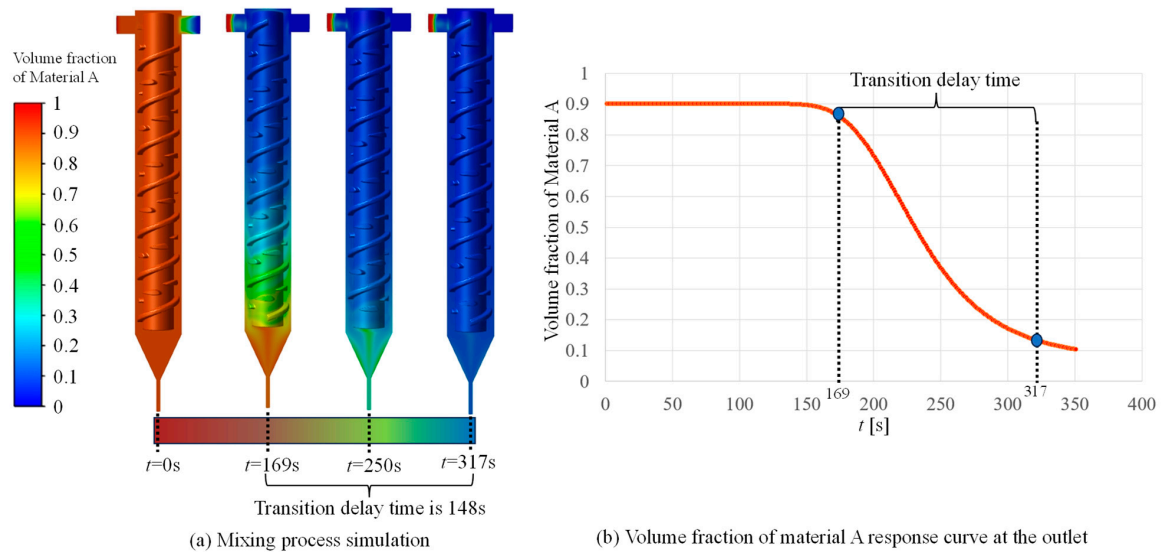


Figure 4. A simulation result of volume fraction change curve of material A (Simulation condition value correspond to Nr.35 experimental design, i.e., the coordinate values for points 1, 2, and 3 are (1.57, 0.74), (1.08, 4.42), and (1.92, 3.58). Response value is 148 s).

Table 5. Coordination values of three points and responses.

Nr.	Point 1	Point 2	Point 3	Delay Time
1	(0.93, 0.36)	(1.92, 3.58)	(1.92, 3.58)	141
2	(1.57, 0.36)	(1.92, 4.42)	(1.92, 3.58)	143
3	(1.25, 0.55)	(1.5, 3)	(1.5, 4)	173
4	(1.57, 0.36)	(1.92, 3.58)	(1.92, 4.42)	175
5	(1.57, 0.74)	(1.08, 3.58)	(1.08, 3.58)	169
6	(1.25, 0.55)	(1.5, 4)	(1.5, 4)	154
7	(0.93, 0.36)	(1.92, 3.58)	(1.08, 4.42)	174
8	(0.5, 0.55)	(1.5, 4)	(1.5, 4)	155
9	(0.93, 0.36)	(1.92, 4.42)	(1.08, 3.58)	151
10	(0.93, 0.74)	(1.08, 4.42)	(1.92, 4.42)	161
11	(1.57, 0.36)	(1.08, 4.42)	(1.08, 3.58)	152
12	(1.57, 0.74)	(1.08, 3.58)	(1.92, 4.42)	174
13	(1.25, 0.55)	(1.5, 4)	(1.5, 5)	187
14	(1.25, 1)	(1.5, 4)	(1.5, 4)	169
15	(0.93, 0.36)	(1.08, 4.42)	(1.08, 4.42)	173
16	(1.25, 0.55)	(1.5, 4)	(1.5, 4)	154
17	(1.57, 0.74)	(1.92, 4.42)	(1.92, 4.42)	156

Table 5. Cont.

Nr.	Point 1	Point 2	Point 3	Delay Time
18	(0.93, 0.36)	(1.92, 4.42)	(1.92, 4.42)	163
19	(0.93, 0.74)	(1.92, 3.58)	(1.08, 3.58)	146
20	(1.57, 0.36)	(1.08, 4.42)	(1.92, 4.42)	161
21	(1.25, 0.55)	(1.5, 4)	(1.5, 4)	154
22	(1.25, 0.55)	(2.5, 4)	(1.5, 4)	150
23	(1.25, 0.55)	(1.5, 4)	(2.5, 4)	148
24	(0.93, 0.36)	(1.08, 3.58)	(1.92, 4.42)	173
25	(1.25, 0.55)	(1.5, 4)	(1.5, 4)	154
26	(1.57, 0.74)	(1.92, 4.42)	(1.08, 3.58)	148
27	(1.25, 0.55)	(1.5, 4)	(1.5, 4)	154
28	(1.57, 0.36)	(1.08, 3.58)	(1.92, 3.58)	158
29	(2, 0.55)	(1.5, 4)	(1.5, 4)	158
30	(1.25, 0.55)	(1.5, 4)	(1.5, 4)	154
31	(1.25, 0.55)	(1.5, 4)	(1.5, 3)	149
32	(0.93, 0.36)	(1.08, 3.58)	(1.08, 3.58)	150
33	(0.93, 0.74)	(1.92, 3.58)	(1.92, 4.42)	171
34	(0.93, 0.74)	(1.08, 3.58)	(1.92, 3.58)	150
35 *	(1.57, 0.74)	(1.08, 4.42)	(1.92, 3.58)	148
36	(0.93, 0.36)	(1.08, 4.42)	(1.92, 3.58)	142
37	(0.93, 0.74)	(1.92, 4.42)	(1.92, 3.58)	142
38	(1.25, 0.55)	(1.5, 4)	(1.5, 4)	154
39	(1.57, 0.74)	(1.92, 3.58)	(1.08, 4.42)	175
40	(1.57, 0.74)	(1.92, 3.58)	(1.92, 3.58)	152
41	(1.57, 0.36)	(1.08, 3.58)	(1.079, 4.42)	179
42	(1.25, 0.55)	(1.5, 4)	(0.5, 4)	160
43	(1.25, 0.55)	(1.5, 5)	(1.5, 4)	148
44	(1.25, 0.1)	(1.5, 4)	(1.5, 4)	170
45	(0.93, 0.74)	(1.08, 3.58)	(1.08, 4.42)	181
46	(1.57, 0.36)	(1.92, 4.42)	(1.08, 4.42)	170
47	(0.93, 0.74)	(1.08, 4.42)	(1.08, 3.58)	149
48	(1.57, 0.74)	(1.08, 4.42)	(1.08, 4.42)	162
49	(1.25, 0.55)	(1.5, 4)	(1.5, 4)	154
50	(0.93, 0.74)	(1.92, 4.42)	(1.08, 4.42)	172
51	(1.57, 0.36)	(1.92, 3.58)	(1.08, 3.58)	160
52	(1.25, 0.55)	(0.5, 4)	(1.5, 4)	157

Nr.35 * simulation results are demonstrated in Figure 4.

The significant modified quadratic response regression model was derived through polynomial regression analysis of the experimental data provided in Table 5, yielding the response function for transition delay time as shown in Equation (5).

$$t_d = 269.39 + 74.38 \times x_1 - 82.55 \times y_1 - 3.28 \times x_2 - 34.88 \times y_2 - 7.11 \times x_3 - 39.62 \times y_3 - 17.68 \times x_1 y_3 - 5.83 \times y_2 y_3 + 73.79 \times y_1^2 + 5.94 \times y_2^2 + 13.44 \times y_3^2 \quad (5)$$

where t_d is transition delay time with a unit of s. The x and y correspond to the coordinate values, respectively, and the foot index represents the serial numbers of the control points.

As seen in Equation (5), it involves all of the first terms of the six factors, along with several interaction and squared terms. Finally, the resulting RSM model fit effect had a

coefficient of determination R^2 of 93.35%, an adjusted coefficient of determination R^2_{adj} of 91.52%, and a predicted determination coefficient R^2_{pre} of 87.5%. This indicates that the model exhibits decent fitting results, and its predictive capability is considered satisfactory. Figures 5 and 6 depict the response surfaces. The remaining four factors were set to intermediate values to generate the response surfaces. In Figure 5a, the x- and y-values represent relative coordinates concerning the third control point. It is evident that changes in the y-value have a more pronounced impact on the response results, with the middle y-values corresponding to a shorter transition delay time. Figure 5b illustrates the response surface for the x- and y-values of the second control point in relation to the transition delay time. Increasing both the x- and y-values results in a lower response value. Figure 5c displays the influence of the x- and y-axis coordinate values of the third control point on the transition delay time. As the x-value increases and the y-value decreases, the response value decreases accordingly. Additionally, Figure 6 represents the effect of changing the two relative coordinates of the first control point with respect to the third point on the transition delay time. It is evident that changes in the y-value exert a more significant impact on the response value compared to changes in the x-value. The minimum response value occurs when the y-value of the third point is at its minimum, and the y-value at the first point is at its middle value. These response surfaces provide valuable insights into the influence of factor variations on response values. Therefore, it is necessary to employ a global optimization approach for the obtained response function to attain specific optimization results.

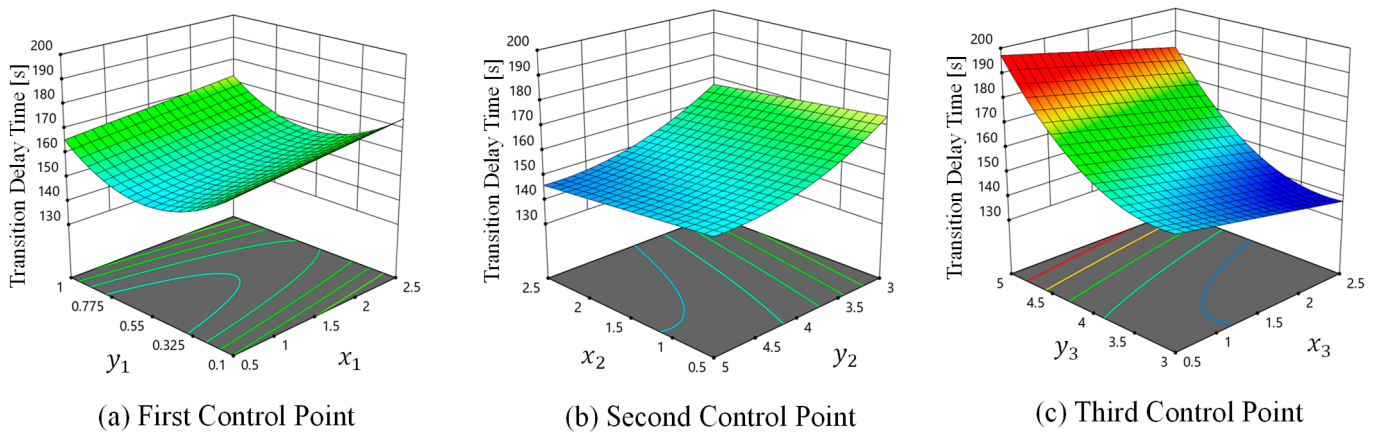


Figure 5. Response surfaces of three control points to transition delay time.

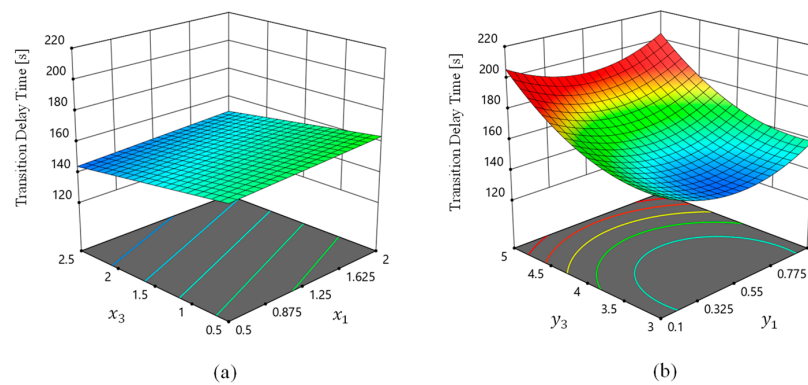


Figure 6. Response surfaces of the first control point with respect to the third control point relative coordinate values to transition delay time. (a) corresponds to the coordinates of x-axis, and (b) is coordinates of y-axis (x_1 and x_3 correspond to the x-coordinate value of the first point and the x-coordinate value of the third point, respectively. y_1 and y_3 correspond to the y-coordinate value of the first point and the y-coordinate value of the third point, respectively).

A genetic algorithm (GA) is a powerful heuristic algorithm used for global search, especially in tackling multivariate and nonlinear optimization problems. A GA emulates the concept of population evolution, employing continuous iterative processes such as selection, crossover, and mutation to gradually transform individuals until the global optimal solution of the problem is achieved.

In this section, Equation (5) is utilized as the response function and optimized using a GA to determine the coordinates of the three control points, aiming to minimize transition delay time. Firstly, the six factors are encoded in binary with a length of 20 bits, establishing the connection between coordinate parameters and the chromosome bit strings' structure in the genetic algorithm. The GA continuously selects and retains individuals with high fitness values for evolutionary processes until convergence is reached. The fitness value is defined based on Equation (5)'s minimum value. We employed a roulette wheel approach to prevent getting trapped in local optimal solutions during the global search. This approach takes into account that individuals with higher fitness values have a greater probability of being selected for further evolution. Additionally, the population size is set to 30, with a maximum of 200 generations. The crossover rate is set to 0.7, and the mutation operator rate is 0.007, ensuring a robust search range and improved convergence speed. The GA execution process is depicted in Figure 7. The results indicate a minimum transition delay time of 117.69 s. The coordinates of the three control points corresponding to this solution are (0.5, 0.56), (2.5, 4.4), and (2.5, 3), while the single pin pattern area is 4.42 mm². Figure 8 displays the optimized pin type screw mixer. Following the optimization results, a simulation of the optimized pin type screw mixer is conducted using the previously defined setup, resulting in a transition delay time of 113 s, which exhibits an acceptable level of error. A detailed numerical verification is presented in the subsequent section.

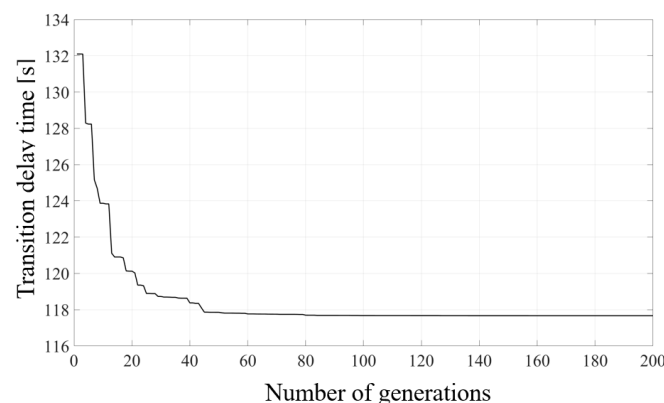


Figure 7. Iteration of objective function.

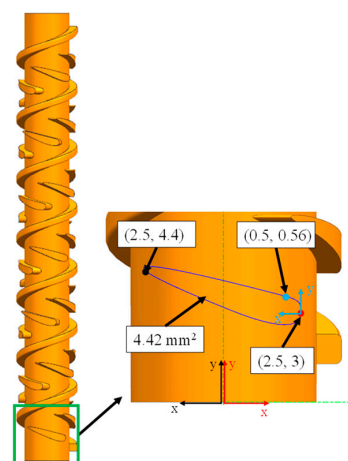


Figure 8. Optimized pin type screw mixer.

3. Results and Discussion

3.1. Numerical Validation

Three different screw configurations were compared to further verify the efficacy of the optimized pinned screw mixer in reducing transition delay time. In addition, the mixing performance of these three screw setups was assessed based on the uniformity of the extruded material and the Lyapunov index. The first screw, illustrated in Table 2 and Figure 9a, represents the original screw without any pins, with its structural parameters, including screw length, pitch, minor screw diameter, and screw flight height, remaining unchanged. Figure 9b showcases the second screw, utilized to demonstrate that the volume in the mixing chamber does not play a decisive role in transition delay times. Custom pins were transformed into cylinders, maintaining the same cross-sectional area and height as the optimized pin-type screw mixer, with a diameter of 2.4 mm and a height of 1 mm. The center of the circle was positioned at the midpoint of the y-axis at an applicable height of (0, 4). The third configuration was the pin-type screw optimized with RSM, as depicted in Figure 8.

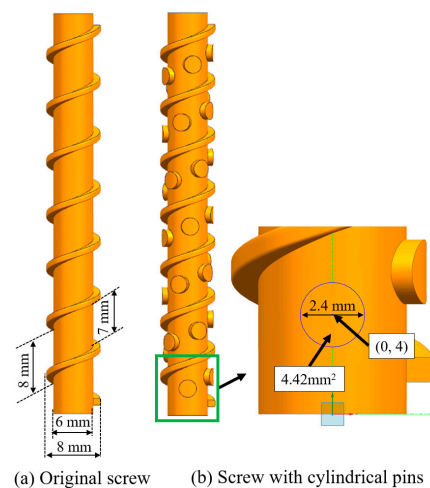


Figure 9. Comparison of screw mixers.

This study then compared the transition delay times of three screw mixers based on the simulation setup detailed in the preceding section. The total flow time was set at 400 s for this analysis. In Figure 10a, we have marked the initial moments when the material A component at the outlet shifted to 0.86 and the termination moments when it reached 0.14. This time interval is defined as the transition delay time. The results reveal that the transition delay time for the optimized pin-type mixer, cylindrical pinned mixer, and pinless mixer stands at 113 s, 158 s, and 169 s, respectively. Notably, compared to the pinless screw mixer, the transition delay time reduced by approximately 33.1%. Moreover, it is evident that, when comparing mixers with the same volume, optimizing the pin shape still reduces the transition delay time by 28.5%. Figure 10b illustrates the probability density curve of the residence time distribution, exhibiting the rate of change of material A's volume fraction at the outlet. The results indicate that the maximum rate of change for the optimized pin-shaped screw mixer reaches 2%/s. In contrast, the corresponding maximum rates of change for the cylindrical pin and the pinless screw are only 1.5%/s and 1.3%/s, respectively. In order to ensure the homogeneity of the printed material, the assessment and monitoring of mixing uniformity at the outlet play a crucial role. The uniformity at the outlet was assessed using the coefficient of variance (COV), defining the extruded mixing material as homogeneous when its value exceeded 95% [51]. As depicted in Figure 11, all three mixers were able to meet the criteria for mixing uniformity at the ratio conversion where mixing difficulty is greatest. However, it is worth noting that the change in uniformity during extrusion was more pronounced for the cylindrical pinned screw and the pinless screw.

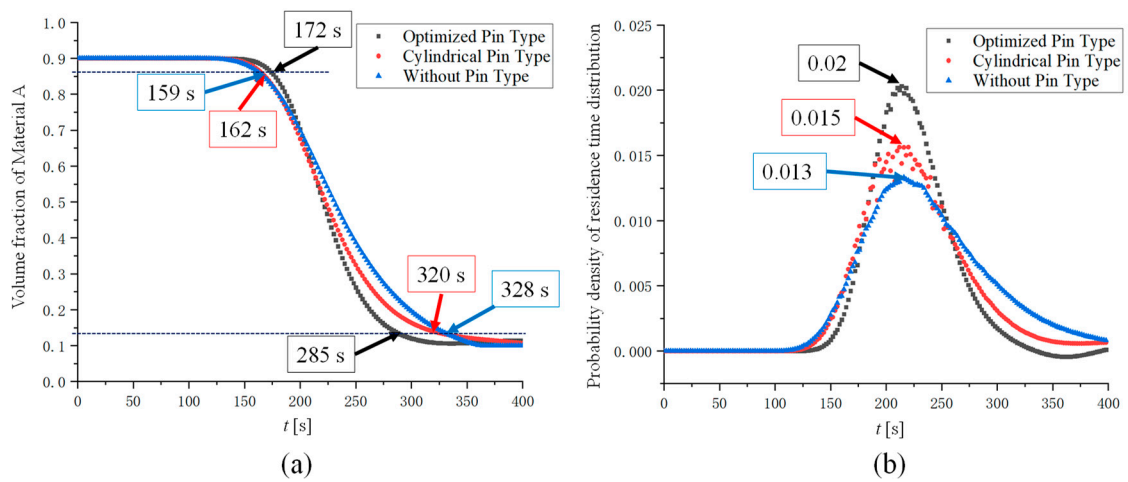


Figure 10. Response curve of three types screw mixer for changes in material A at the outlet. (a) is the curve of change in volume fraction of material A at the outlet, and (b) is the probability density function of residence time distribution.

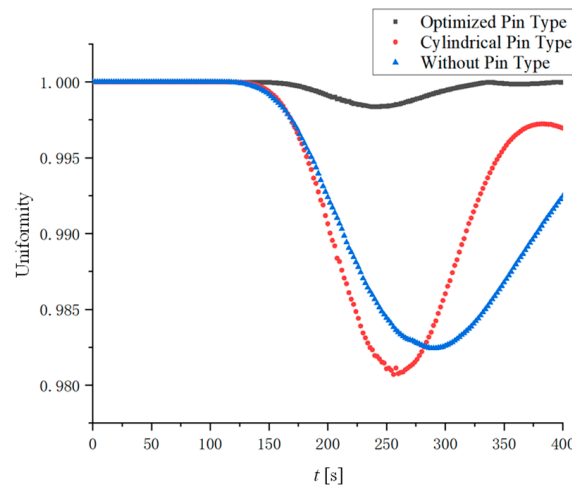


Figure 11. Uniformity curve at the outlet.

Five randomly selected particles’ trajectories were tracked from the two inlet points of the three screw types using ANSYS FLUENT Vision 2020R2 (fluid simulation software) to evaluate and compare the efficacy of the optimized pin shape in enhancing the chaotic mixing of the two paste-like substances in the chamber. This tracking yielded the spatial coordinates of the particles as they evolved over time. Analysis of the particle trajectories, as depicted in Figure 12, reveals a higher degree of chaos associated with the optimized pin-type mixer. Moreover, the level of chaotic mixing was quantified using Equation (6)’s Lyapunov exponent.

$$\lambda = \lim_{\substack{t \rightarrow \infty \\ \Delta x \rightarrow 0}} \frac{1}{t} \ln \frac{|\Delta x(t)|}{|\Delta x(0)|} \tag{6}$$

where $\Delta x(0)$ is the separation of the two particles at the initial time and $\Delta x(t)$ represents the separation at time t .

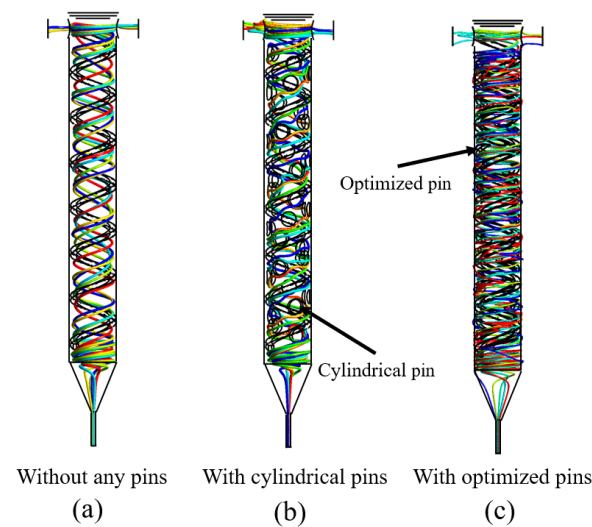


Figure 12. Path line of five random particles in the mixing chamber.

Moreover, the degree of chaotic mixing was quantified through the utilization of Equation (6), which calculates the Lyapunov exponent. A larger positive Lyapunov exponent signifies a more pronounced level of chaotic mixing. During the Lyapunov exponent calculation process, particles with close initial distances were selected as clusters, utilizing the spatial coordinates of the five randomly tracked particles over time, as previously described. The sampling frequency was set at 1 Hz, with a mixing period of 100 s. Each screw type yielded five sets of Lyapunov exponents, which were averaged to characterize the final degree of chaotic mixing, as presented in Table 6. The results clearly demonstrate that the optimized mixer generates over three times the level of chaotic mixing compared to the other two screw types.

Table 6. Lyapunov exponents of each screw mixer.

	Screw without Pins	Screw with Cylindrical Pins	Screw with Optimized Pins
Lyapunov exponents	0.007833	0.00965	0.03402

Figure 13 illustrates the Poincaré map representing the behavior of two isolated particles influenced by the presence of three screws over flow durations of 100 s and 200 s. The x and y coordinates on the Poincaré map represent the specific positions of these particles. The findings demonstrate that a screw devoid of pins and a screw equipped with symmetrically shaped pins yield similar cross-sectional flow trajectories for the two separated particles. This similarity has a detrimental effect on radial mixing. A comparison between Figure 13c,f shows that the optimized pin shape mixer allows the two separated particles more uniformly distributed in the radial direction of the mixing chamber after 100 s of mixing. Moreover, it is observed that the trajectories of these particles exhibit increased chaotic behavior in the cross-section of the optimized pinned screw. This results in a higher number of cross-foldings and, thus, enhances homogeneity in the extrusion process. Thus, it is verified that the optimization-induced asymmetry in the pin shape allows the mixing fluid to continuously overlap and merge after passing through the upper and lower surfaces of the pin. This phenomenon enhances chaotic convection in the mixing chamber, thereby enhancing radial mixing and reducing axial mixing. Finally, this leads to a reduction in the transition delay time.

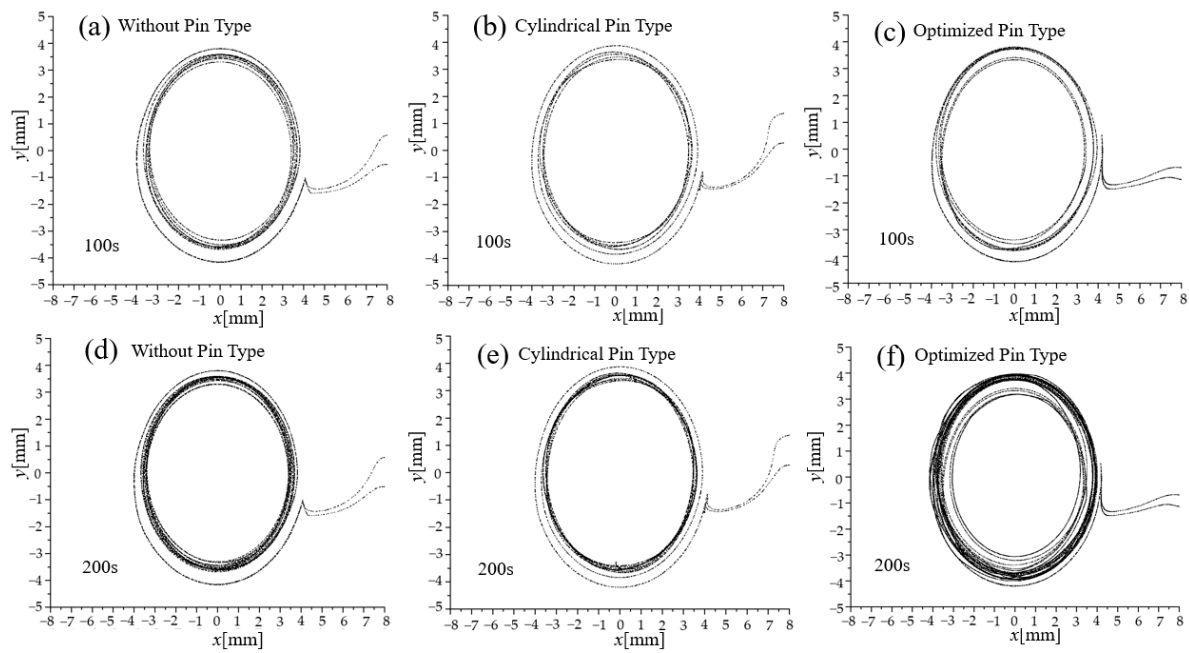


Figure 13. Poincaré map of three screw mixers at different flow times.

3.2. Printing System

Figure 14 illustrates a custom-built printing prototype designed for the preparation of FGM parts. This prototype comprises two primary modules: the data processing module and the spatial motion module. The data processing module serves the function of receiving and analyzing G-codes containing printing information, following the slicing process, facilitated by the upper computer. Thereafter, it translates these G-codes into pulse signals compatible with each motor of the printer. This conversion enables accurate execution of the printing procedure. The spatial motion module, on the other hand, is composed of two principal components, with one being a triaxial gantry structure. A layer-based manufacturing approach is employed to ensure the geometric accuracy of the FGMs parts. The 42-stepping motor can provide a maximum torque of 0.5 Nm. Equipped with a ball screw shaft with lead of 10 mm, a single 42 stepper motor can provide a force of 35 N (seen in Equation (7)).

$$F = \frac{2T}{0.9L\pi} \tag{7}$$

where T is the maximum torque of motor, and L is the lead of ball screw shaft.

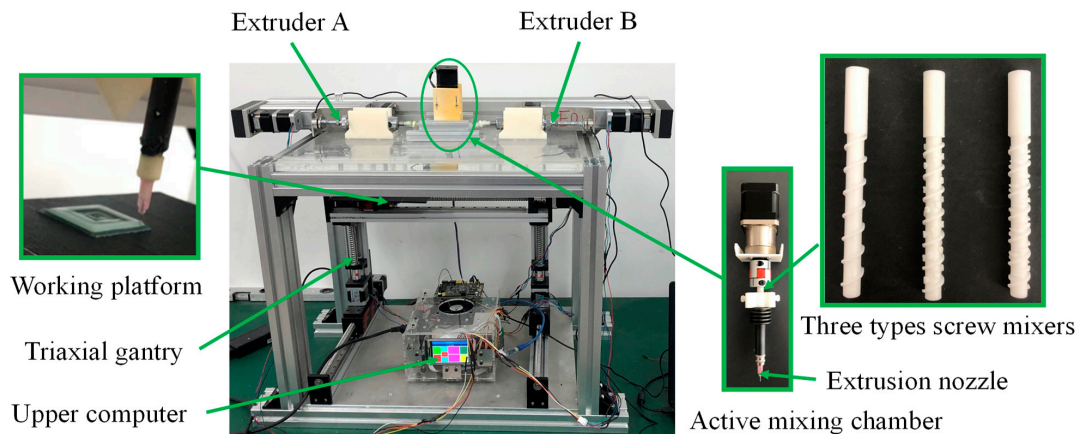


Figure 14. Printing prototype for fabrication of FGM parts.

Therefore, we used double 42-stepping motors into the y-axis and z-axis to ensure sufficient torque, while the x-axis is driven by a single 42-stepping motor. Moreover, this module features a unique component to facilitate variations in material composition, comprising two extruders and an active mixing chamber. Extruder A and extruder B are each equipped with separate 42-stepping motors, enabling the manipulation of material gradients through different feed rates. In the feeding system, in addition to the 42-stepping motors fitted with 10 mm lead ball screws, a 10:1 reducer is also equipped, allowing a maximum thrust of 350 N to be provided by a single motor. Measured via a pressure sensor during the printing process, the required thrust force is about 200 N when feeding at the maximum feed rate of 0.5 mm/s. The screw mixer housed in the active mixing chamber is connected via a coupling to a 42-step motor, and the motor is equipped with a gearbox with a transmission ratio of 10:1 in order to provide sufficient torque for mixing. During the printing experiment, we set the screw to rotate at 25 rpm to match the simulation settings. Figure 14 also presents three screw mixers, which were produced using 3D printing in combination with high strength resins based on the parameters outlined in the previous section. These mixers are intended for use in subsequent practical printing experiments to assess print quality.

3.3. Verification Experiment

With the aforementioned internally developed printing system equipped with three types of mixers, the response was the printing of a $70 \times 70 \text{ mm}^2$ extruded filament displaying gradient variations from 90% of material A (white color) to 10% of material B (green color), and vice versa, as illustrated in Figure 15. Prior to the experiment, the two extruders were supplied in accordance with the initial paste ratio (9:1), and the screw speed was adjusted to 25 rpm for purging the mixing chamber. Thereafter, the dual extruders were supplied at the desired ratio (1:9) until the filament was produced. The printing path followed a zigzag pattern with 5 mm intervals, with the starting point indicated by the arrow in Figure 15. The total length of the extruded filament amounted to 1120 mm. The experimental printing parameters were configured to match the simulation settings. The extrusion head diameter remained at 1 mm, the combined feed rate was 0.5 mm/s, and the extruded flow rate from the nozzle could be estimated at approximately $2.4 \text{ mm}^3/\text{s}$. Therefore, to ensure the absence of noticeable overstacking and understacking defects in the printing process, the movement speed of the printing platform was set to approximately 3 mm/s, following the principles of flow conservation. Therefore, the total printing time for the extruded filaments was 373 s. Hence, the transitional delay distance can be computed based on the platform's movement speed combined with the transition delay time.

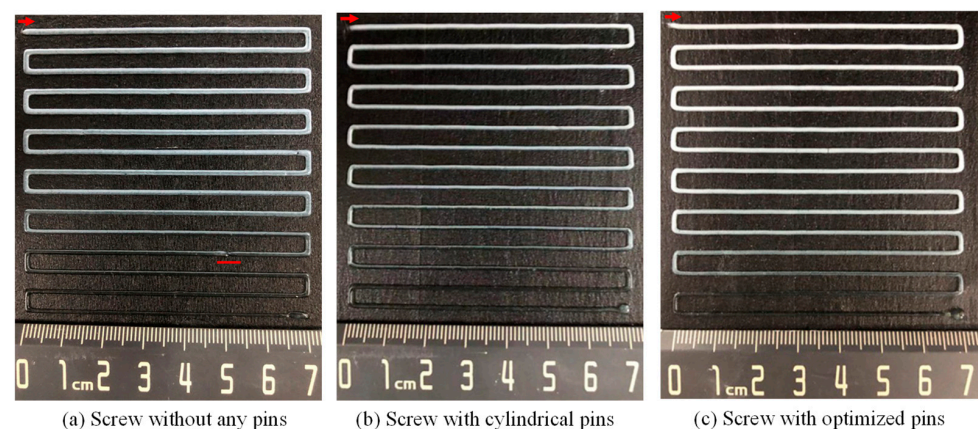


Figure 15. Three mixers extruded filaments with gradient variations.

As depicted in Figure 15, all three mixers are capable of inducing gradient changes in the extruded filaments while maintaining satisfactory geometric print quality. Notably, as

highlighted in Figure 15a, filament breakage is evident, primarily attributed to the introduction of air bubbles during the loading of paste-like material into the extruder. Mixers lacking pins exhibit suboptimal dispersal and mixing capabilities, with minimal change in the size of the entrapped bubbles. The occurrence of these bubbles during material loading proves challenging to circumvent, and their dimensions directly impact filament breakage. Therefore, increased volumes of bubbles result in geometric inaccuracies during the printing process and exert a negative effect on the mechanical characteristics of the FGM parts. Conversely, when air bubbles infiltrate screw configurations equipped with pins, the larger bubbles can be dispersed into smaller units through the multiple shearing actions of the pins. This, in turn, translates into enhanced geometric quality, as illustrated in Figure 15b,c.

3.4. Comparison of Transition Delay Distances

It is evident that utilizing image processing methods offers a cost-effective approach for detecting gradient variations in extrusion filament. Firstly, the printed output displayed in Figure 15 was processed through the MATLAB platform and transformed into a grayscale representation to obtain the grayscale value for each individual pixel. Secondly, pixel coordinates were determined based on the locations of sampling points in the grayscale map presented in Figure 16, and the normalized values were characterized as the composition ratio at each of these sampling points. A total of 113 sampling points were acquired, employing a uniform sampling strategy aligned with the length of the extruded filaments, which resulted in a cumulative printing duration of 373 s. Finally, a comparative analysis was conducted between the experimental results and the CFD results, as illustrated in the coordinate system of Figure 16. Additionally, the commencement and conclusion points of the transition delay time for three mixers, as determined using the CFD results, are denoted in Figure 16.

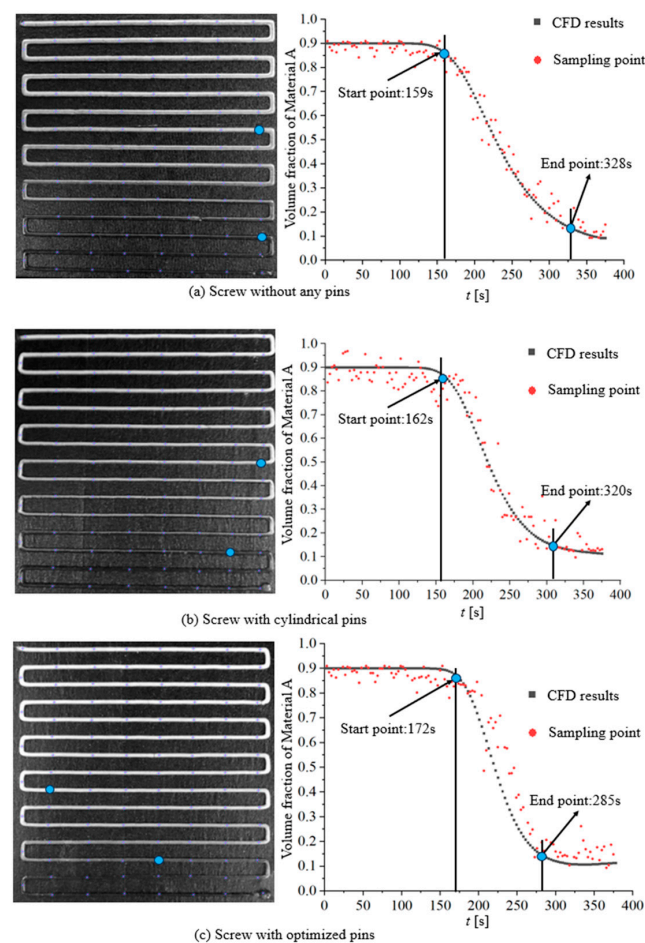


Figure 16. Digital image processing of three print filaments.

From the findings presented in Figure 16, it is evident that all three mixers have the capability to change the gradient of material components in an extruded filament spanning 1120 mm, ranging from a ratio of 9:1 to 1:9. The complete transformation of material components is readily observable through digital image processing methods. Moreover, when comparing the experimental results with those derived from CFD simulations, it is apparent that the simulation results exhibit acceptable deviations, thereby establishing the validity and reasonable accuracy of the FEM model in the context of the mixing process.

In Figure 16a, the analysis results depict the extruded filaments produced by the screw mixer devoid of any pins. The grey values of the sampled points in the transition delay interval are evenly distributed on either side of the CFD results, signifying a considerable delay in the transition process. In Figure 16b, a comparison with the CFD results reveals that the presence of pins in actual printing only marginally enhances the effects of chaotic mixing convection, resulting in a tendency to delay the transformation of material components during practical use. In Figure 16c, the grey scale values of the sampled points from the experiment surpass the CFD results, indicating that in practice, the screw with the optimized pin shape significantly promotes chaotic mixing, leading to shorter transition distances for material gradient changes. This smooth transition of material components in functional gradient materials can substantially reduce interlayer stresses induced by abrupt shifts in material properties, thus enhancing the overall structural integrity and durability of the component. The reduced transition distance allows for more complex and accurate material gradient adjustments between layers in confined dimensions, thereby enhancing printing flexibility and enabling the design of FGM parts that transcend dimensional limitations. This not only maximizes the unique advantages of individual component materials but also offers a wider range of performance combinations.

3.5. Functionally Graded Materials Part Print Specimen

We printed a $35 \times 35 \times 3.2 \text{ mm}^3$ cube with a gradient variation to verify the printing performance of the optimized pin screw mixer, as illustrated in Figure 17. Each layer was set to a height of 0.8 mm, and a consistent gradient change was maintained in each layer. The printing path followed an offset printing sequence, progressing from the outermost to the innermost regions, and was accompanied by a 100% fill rate. Figure 17a illustrates the gradient variation of the pre-designed printed sample, where the region denoted as 6:4 measures 2 mm in width, the 9:1 region spans 3 mm in width, and the central region accounts for a component ratio of 1.5:8.5. To account for the delay in material component transformation once the printing system receives the G-Code, the mixing chamber was initially purged with a mixture of pastes in a 6:4 ratio before commencing printing. Printing commenced with G-Code specifying a material ratio of 9:1 and continued until the next ratio change point, i.e., (30, 5). From that point onward, the ratio was adjusted to 1.5:8.5 until the completion of the layer. Figure 17b displays the specimen that was printed following the predefined G-Codes and the associated process parameters from the aforementioned experiment. The print results indicate that the specimen exhibits satisfactory surface quality.

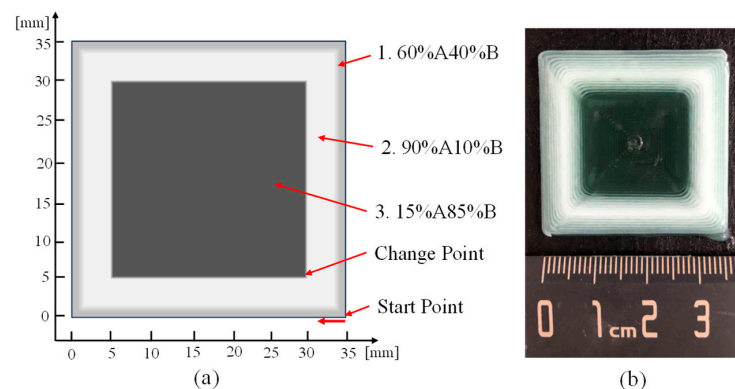


Figure 17. Illustration of: (a) pre-designed gradient change, and (b) print specimen.

Similarly, digital image processing was employed to analyze the gradient variations of the printed sample in a targeted manner. Sampling components along the designated arrow paths in the greyscale diagram presented in Figure 18 and subsequently comparing them with the expected gradient changes revealed that the transitional region between the ratios of 6:4 and 9:1 spanned approximately 2 mm. In addition, the width of this transition region measured approximately 5 mm after the material feed transition point, set at a ratio of 1.5:8.5. In summary, the optimized pin screw mixer demonstrates a significant capability to achieve the distribution of components as pre-designed.

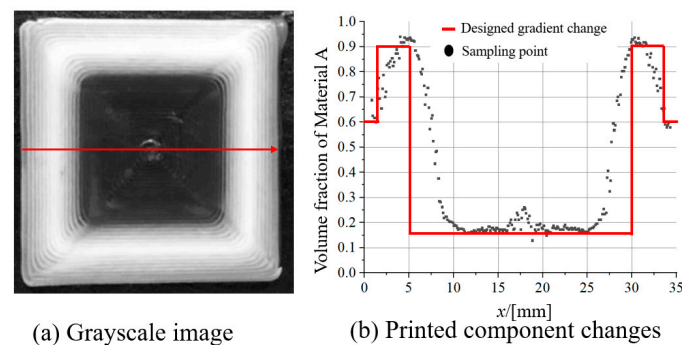


Figure 18. Digital image processing of print specimen.

Direct ink writing, a sophisticated additive manufacturing method, offers remarkable flexibility and adaptability. This method excels in accurately depositing materials at predetermined locations to create complex geometries and complex structures. However, a significant challenge encountered when preparing FGMs parts with the DIW process is the unavoidable formation of transition delay regions. While these regions may not be functionally critical, they can exert a significant effect on the overall performance of the manufactured parts. Further research should focus on the development of more efficient path planning strategies, along with accurate characterization of the transition delay distances between varying gradient variations. By strategically placing these transition delay regions in non-core functional areas of the part, it is possible to enhance overall part performance and quality without compromising critical functionality.

In this study, we have successfully determined a pin shape for single-screw mixer by virtue of chaotic mixing, combined with several digital optimization techniques. Experimental validation shows that the optimized active screw mixer can effectively shorten the transition delay distance, as well as achieve sufficient distribution mixing capacity, when the material components are transformed. Finally, we successfully prepared printed samples with gradient changes with the optimized screw, which will help the application development in the field of functional gradient materials.

4. Conclusions

The pin-type active screw mixer, developed utilizing RSM in conjunction with a global optimization approach, has proven its efficacy in substantially reducing the distance required for the transition of material components. When compared to two other similar screw types, the optimized pin-type screw mixer reduced the transition distance by approximately 28.5% and 33.1%, respectively, in scenarios where the ratio of material component changes ranged from 9:1 to 1:9. In addition, CFD models with a high degree of accuracy have been generated in this study. These models are unquestionably capable of efficiently and economically characterizing the transition delay time for material component changes and the uniformity of mixing in extruded materials. In conjunction with the simulation results, the response function of the three control points to the transition delay time was eventually determined through the half-composite center design. In the simulation model, the particle tracking method was employed to compute the Lyapunov exponent, which serves to assess the degree of chaotic mixing in the chamber. Additionally, this method

evaluates the radial dispersive mixing capability of the mixer through the Poincaré map. Numerical validation results indicate that the Lyapunov exponent of the optimized pin-type screw mixer is 4.3 times higher than that of the mixer lacking pins and 3.5 times higher than that of the cylindrical pinned mixer. The Poincaré map further confirms that the optimized pin-type screw offers superior radial dispersion mixing capabilities. These findings provide evidence that the optimized pin-type screw mixer enhances the chaotic mixing effect by increasing radial mixing while decreasing axial mixing. Through experimental research, the double-extruder printing system, combined with the optimized screw mixer, has successfully prepared FGM parts with smooth variations. Moreover, the gradient change process can be effectively characterized through digital image processing.

In this work, the researchers extensively studied a singular instance of transition delay distance associated with a change in material components. In addition, the CFD model can be employed to explore additional transition delay distances arising from various changes in material components. To streamline the experimental data, this study utilized a quadratic B-spline to characterize the pin's geometry. Subsequent research may involve the utilization of higher-degree B-splines to extend the scope of design possibilities. It is worth noting that nearly all paste-like materials are amenable to the DIW process. This presents exciting opportunities for further exploration into the regulation of printing parameters for pastes exhibiting diverse rheological properties, such as ceramics, polymers, and other non-Newtonian fluids. This exploration holds the potential to unlock a wider array of performance of FGM parts. Regarding the study of print path strategies, future research directions may consist of the consideration of the spatial deployment of the transition region. The objective would be to achieve a transition while minimizing any negative effects on material properties.

Author Contributions: All authors contributed to the study conception and design; The draft of the manuscript was written by S.W.; All authors were involved in analysing the data. J.Z. reviewed this paper; G.D. provided the management for the work. All authors have read and agreed to the published version of the manuscript.

Funding: This project was supported by the Central Guidance for Local Science and Technology Development Fund Project, Hebei Provincial Department of Science and Technology, China (Grant No. 216Z1804G).

Institutional Review Board Statement: Not applicable.

Informed Consent Statement: Not applicable.

Data Availability Statement: Data are contained within the article.

Conflicts of Interest: The authors declare no conflicts of interest.

References

1. Jojith, R.; Sam, M.; Radhika, N. Recent advances in tribological behavior of functionally graded composites: A review. *Eng. Sci. Technol. Int. J.* **2022**, *25*, 100999. [[CrossRef](#)]
2. Kumar, J.; Singh, D.; Kalsi, N.S.; Sharma, S.; Pruncu, C.I.; Pimenov, D.Y.; Rao, K.V.; Kapłonek, W. Comparative study on the mechanical, tribological, morphological and structural properties of vortex casting processed, Al-SiC-Cr hybrid metal matrix composites for high strength wear-resistant applications: Fabrication and characterizations. *J. Mater. Res. Technol.* **2020**, *9*, 13607–13615. [[CrossRef](#)]
3. Dmitrievskiy, A.A.; Zhigacheva, D.G.; Grigoriev, G.V. Ca-ATZ/Ca-ATZ+SiO₂ functionally graded ceramic. *Adv. Appl. Ceram.* **2023**, *122*, 31–35. [[CrossRef](#)]
4. Osman, S.; Ahmed, K.; Ahmed, M. Performance of Two-Dimensional Functionally Graded Anode Supported Solid-Oxide Fuel Cells. *J. Energy Resour. Technol.* **2022**, *144*, 070911. [[CrossRef](#)]
5. Verma, R.K.; Chopkar, M.K. Dry Sliding Wear Investigation of Centrifugally Casted AA6061–B4C Functionally Graded Metal Matrix Composite Material by Response Surface Methodology (RSM). *Arab. J. Sci. Eng.* **2023**, *48*, 4095–4107. [[CrossRef](#)]
6. Huang, C.; Chen, Y. Effect of varied alumina/zirconia content on ballistic performance of a functionally graded material. *Int. J. Refract. Met. Hard Mater.* **2017**, *67*, 129–140. [[CrossRef](#)]
7. Huang, C.-Y.; Chen, Y.-L. Design and impact resistant analysis of functionally graded Al₂O₃–ZrO₂ ceramic composite. *Mater. Des.* **2016**, *91*, 294–305. [[CrossRef](#)]

8. Huang, C.-Y.; Chen, Y.-L. Effect of mechanical properties on the ballistic resistance capability of Al₂O₃-ZrO₂ functionally graded materials. *Ceram. Int.* **2016**, *42*, 12946–12955. [[CrossRef](#)]
9. Coffigniez, M.; Grémillard, L.; Boulnat, X. Sinter-Based Additive Manufacturing of Graded Porous Titanium Scaffolds by Multi-Inks 3D Extrusion. *Adv. Eng. Mater.* **2022**, *25*, 2201159. [[CrossRef](#)]
10. George, S.M.; Nayak, C.; Singh, I.; Balani, K. Multifunctional Hydroxyapatite Composites for Orthopedic Applications: A Review. *ACS Biomater. Sci. Eng.* **2022**, *8*, 3162–3186. [[CrossRef](#)]
11. Zhang, Y.B.; Yang, H.L.; Lei, S.Q.; Zhu, S.J.; Wang, J.F.; Sun, Y.F.; Guan, S.K. Preparation of Biodegradable Mg/β-TCP Biofunctional Gradient Materials by Friction Stir Processing and Pulse Reverse Current Electrodeposition. *Acta Metall. Sin. (Engl. Lett.)* **2020**, *33*, 103–114. [[CrossRef](#)]
12. Wang, Y.; Liu, Q.; Lan, Z.-F.; Zhang, B.; Zhang, H.-Q.; Liu, J.-W.; Ye, F. Strong and tough bioinspired nacre-like B₄C/Al functionally graded materials with eliminated abrupt interfaces. *Compos. Commun.* **2021**, *25*, 100741. [[CrossRef](#)]
13. Caño, P.; Hinojosa, M.; Nguyen, H.; Morgan, A.; Fuertes Marrón, D.; García, I.; Johnson, A.; Rey-Stolle, I. Hybrid III-V/SiGe solar cells grown on Si substrates through reverse graded buffers. *Sol. Energy Mater. Sol. Cells* **2020**, *205*, 110246. [[CrossRef](#)]
14. Du, J.; Zhou, Z.J.; Song, S.X.; Zhong, Z.H.; Ge, C.C. Research on Mo/Cu functionally graded materials by resistance sintering under ultra-high pressure. *AIP Conf. Proc.* **2008**, *973*, 862–867. [[CrossRef](#)]
15. Hurdoganoglu, D.; Safaei, B.; Sahmani, S.; Onyibo, E.C.; Qin, Z. State-of-the-Art Review of Computational Static and Dynamic Behaviors of Small-Scaled Functionally Graded Multilayer Shallow Arch Structures from Design to Analysis. *Arch. Comput. Methods Eng.* **2023**, *31*, 389–453. [[CrossRef](#)]
16. Srividhya, S.; Raghu, P.; Rajagopal, A.; Reddy, J.N. Nonlocal nonlinear analysis of functionally graded plates using third-order shear deformation theory. *Int. J. Eng. Sci.* **2018**, *125*, 1–22. [[CrossRef](#)]
17. Jeshrun Shalem, M.; Devaraju, A.; Karthik, K. Synthesis and Characterization of Functionally Graded Ceramic Material for Aerospace Applications. In *Intelligent Manufacturing and Energy Sustainability*; Springer: Singapore, 2020; pp. 483–488. [[CrossRef](#)]
18. Kumar, S.; Reddy, K.V.V.S.M.; Kumar, A.; Devi, G.R. Development and characterization of polymer-ceramic continuous fiber reinforced functionally graded composites for aerospace application. *Aerosp. Sci. Technol.* **2013**, *26*, 185–191. [[CrossRef](#)]
19. Ramesh, M.; Karthik, A.; Jafrey Daniel James, D.; Karthik Pandiyan, G. Functionally graded materials: Review on manufacturing by Liquid and gas based techniques. *Mater. Res. Express* **2023**, *10*, 085305. [[CrossRef](#)]
20. Ren, L.; Song, Z.; Liu, H.; Han, Q.; Zhao, C.; Derby, B.; Liu, Q.; Ren, L. 3D printing of materials with spatially non-linearly varying properties. *Mater. Des.* **2018**, *156*, 470–479. [[CrossRef](#)]
21. Yang, L.; Miyanaji, H.; Janaki Ram, D.; Zandinejad, A.; Zhang, S. Functionally Graded Ceramic Based Materials Using Additive Manufacturing: Review and Progress. *Addit. Manuf. Strateg. Technol. Adv. Ceram.* **2016**, *258*, 43–55. [[CrossRef](#)]
22. Eriskin, C.; Kalyon, D.M.; Wang, H. Functionally graded electrospun polycaprolactone and β-tricalcium phosphate nanocomposites for tissue engineering applications. *Biomaterials* **2008**, *29*, 4065–4073. [[CrossRef](#)] [[PubMed](#)]
23. Brackett, J.; Yan, Y.; Cauthen, D.; Kishore, V.; Lindahl, J.; Smith, T.; Sudbury, Z.; Ning, H.; Kunc, V.; Duty, C. Characterizing material transitions in large-scale Additive Manufacturing. *Addit. Manuf.* **2021**, *38*, 101750. [[CrossRef](#)]
24. Guo, W.; Jiang, Z.; Zhang, C.; Zhao, L.; Jiang, Z.; Li, X.; Chen, G. Fabrication process of smooth functionally graded materials through a real-time inline control of the component ratio. *J. Eur. Ceram. Soc.* **2021**, *41*, 256–265. [[CrossRef](#)]
25. Tang, D.; Hao, L.; Li, Y.; Li, Z.; Dadbakhsh, S. Dual gradient direct ink writing for formation of kaolinite ceramic functionally graded materials. *J. Alloys Compd.* **2020**, *814*, 152275. [[CrossRef](#)]
26. Li, W.; Armani, A.; Martin, A.; Kroehler, B.; Henderson, A.; Huang, T.; Watts, J.; Hilmas, G.; Leu, M. Extrusion-based additive manufacturing of functionally graded ceramics. *J. Eur. Ceram. Soc.* **2021**, *41*, 2049–2057. [[CrossRef](#)]
27. Netto, J.M.J.; Idogava, H.T.; Santos, L.E.F.; Silveira, Z.D.; Romio, P.; Alves, J.L. Screw-assisted 3D printing with granulated materials: A systematic review. *Int. J. Adv. Manuf. Tech.* **2021**, *115*, 2711–2727. [[CrossRef](#)] [[PubMed](#)]
28. Valkenaers, H.; Vogeler, F.; Ferraris, E.; Voet, A.; Kruth, J.P. A novel approach to additive manufacturing: Screw extrusion 3D-printing. In Proceedings of the International Conference on Multi-Material Micro Manufacture, San Sebastián, Spain, 8–10 October 2013.
29. Cartwright, J.H.E.; Feingold, M.; Piro, O. An Introduction to Chaotic Advection. In *Mixing: Chaos and Turbulence*; Chaté, H., Villiermaux, E., Chomaz, J.M., Eds.; Springer: Boston, MA, USA, 1999; pp. 307–342.
30. Castelain, C.; Mokrani, A.; Legentilhomme, P.; Peerhossaini, H. Residence time distribution in twisted pipe flows: Helically coiled system and chaotic system. *Exp. Fluids* **1997**, *22*, 359–368. [[CrossRef](#)]
31. Aref, H. Stirring by chaotic advection. *J. Fluid Mech.* **1984**, *143*, 1–21. [[CrossRef](#)]
32. Sundararajan, P.; Stroock, A. Transport Phenomena in Chaotic Laminar Flows. *Annu. Rev. Chem. Biomol. Eng.* **2012**, *3*, 473–496. [[CrossRef](#)]
33. Xu, B.; Liu, Y.; Yu, H.; Turng, L.; Liu, C. A Numerical Simulation of Enhanced Mixing of a Non-Newtonian Fluid in a Cavity with Asymmetric Non-Twin Rotors. *Macromol. Theory Simul.* **2018**, *27*, 1800021. [[CrossRef](#)]
34. Xu, B.; Liu, Y.; He, L.; Turng, L.; Liu, C. Effect of centerline distance on mixing of a Non-Newtonian fluid in a cavity with asymmetric rotors. *Phys. Fluids* **2018**, *31*, 021205. [[CrossRef](#)]
35. Wei, J.J.; Liang, X.L.; Chen, D.; Yang, Y.; Zhou, D.M. Evaluation of the mixing performance for one novel twin screw kneader with particle tracking. *Polym. Eng. Sci.* **2014**, *54*, 2407–2419. [[CrossRef](#)]

36. Wei, J.; Sun, Q.; Sun, X.; Sun, W. A study on rotor profiles design for a novel twin-screw kneader. *Int. J. Precis. Eng. Manuf.* **2013**, *14*, 451–459. [[CrossRef](#)]
37. Zhu, X.Z.; He, Y.D.; Wang, G. Effect of Dynamic Center Region on the Flow and Mixing Efficiency in a New Tri-Screw Extruder Using 3D Finite Element Modeling. *Int. J. Rotating Mach.* **2013**, *2013*, 258197. [[CrossRef](#)]
38. Bauer, H.; Matic, J.; Khinast, J. Characteristic parameters and process maps for fully-filled twin-screw extruder elements. *Chem. Eng. Sci.* **2021**, *230*, 116202. [[CrossRef](#)]
39. Bhattacharyya, A.; Janarthanan, G.; Tran, H.N.; Ham, H.J.; Yoon, J.; Noh, I. Bioink homogeneity control during 3D bioprinting of multicomponent micro/nanocomposite hydrogel for even tissue regeneration using novel twin screw extrusion system. *Chem. Eng. J.* **2021**, *415*, 128971. [[CrossRef](#)]
40. Kohlgrüber, K. 4—Applications of Co-Rotating Twin-Screw Extruders. In *Co-Rotating Twin-Screw Extruders: Applications*; Kohlgrüber, K., Ed.; Hanser: Pawleys Island, SC, USA, 2021; pp. 217–339.
41. Kim, S.J.; Kwon, T.H. Enhancement of mixing performance of single-screw extrusion processes via chaotic flows: Part I. Basic concepts and experimental study. *Adv. Polym. Technol.* **1996**, *15*, 41–54. [[CrossRef](#)]
42. Kim, S.J.; Kwon, T.H. Enhancement of mixing performance of single-screw extrusion processes via chaotic flows: Part II. Numerical study. *Adv. Polym. Technol.* **1996**, *15*, 55–69. [[CrossRef](#)]
43. Hwang, W.R.; Kwon, T.H. Dynamical modeling of chaos single-screw extruder and its three-dimensional numerical analysis. *Polym. Eng. Sci.* **2000**, *40*, 702–714. [[CrossRef](#)]
44. Wiggins, S.; Ottino, J. Foundation of chaotic mixing. *Philos. Transactions. Ser. A Math. Phys. Eng. Sci.* **2004**, *362*, 937–970. [[CrossRef](#)]
45. Park, G.; Eom, T.; Kwak, H.; Kim, C. Optimization of Screw Mixer to Improve Drying Performance of Livestock Manure Dryer Using CFD Analysis. *Appl. Sci.* **2022**, *12*, 2872. [[CrossRef](#)]
46. Shankar, T.J.; Sokhansanj, S.; Bandyopadhyay, S.; Bawa, A.S. A Case Study on Optimization of Biomass Flow During Single-Screw Extrusion Cooking Using Genetic Algorithm (GA) and Response Surface Method (RSM). *Food Bioprocess Technol.* **2010**, *3*, 498–510. [[CrossRef](#)]
47. Liu, T.; Wang, J.; Li, Y.; Liu, Z.; Sun, J.; Liu, D. Design and Experiment of Substrate Grass Seed Blanket Extrusion Device. *Sustainability* **2022**, *14*, 11046. [[CrossRef](#)]
48. Phelan Jr, F.; Hughes, N.; Pathak, J. Chaotic Mixing in Microfluidic Devices Driven by Oscillatory Cross Flow. *Phys. Fluids* **2008**, *20*, 023101. [[CrossRef](#)]
49. Orisaleye, J.; Adefuye, O.; Ogundare, A.; Fadipe, O. Parametric analysis and design of a screw extruder for slightly non-Newtonian (pseudoplastic) materials. *Eng. Sci. Technol. Int. J.* **2018**, *21*, 229–237. [[CrossRef](#)]
50. Rauwendaal, C. (Ed.) 7—Functional Process Analysis. In *Polymer Extrusion*, 5th ed.; Hanser: Pawleys Island, SC, USA, 2014; pp. 255–508.
51. Hosseini, S.M.; Razzaghi, K.; Shahraki, F. Design and characterization of a Low-pressure-drop static mixer. *AIChE J.* **2019**, *65*, 1126–1133. [[CrossRef](#)]

Disclaimer/Publisher’s Note: The statements, opinions and data contained in all publications are solely those of the individual author(s) and contributor(s) and not of MDPI and/or the editor(s). MDPI and/or the editor(s) disclaim responsibility for any injury to people or property resulting from any ideas, methods, instructions or products referred to in the content.